Nuclear Instruments and Methods in Physics Research A 344 (1994) 492–506
North-Holland

NUCLEAR INSTRUMENTS & METHODS IN PHYSICS RESEARCH
Section A

Electron/pion separation with the H1 LAr calorimeters

H1 Calorimeter Group

B. Andrieu [j], J. Bán [f], E. Barrelet [k], G. Bernardi [k], M. Besançon [d], E. Binder [e], H. Blume [h], K. Borras [c], V. Boudry [j], V. Brisson [i], A. Campbell [e], T. Carli [h], M. Colombo [c], Ch. Coutures [d], G. Cozzika [d], J. Cvach [j], M. David [d], L. Del Buono [k], B. Delcourt [i], M. Devel [i], P. Dingus [j], A. Drescher [c], J. Duboc [k], R. Ebbinghaus [c], S. Egli [n], J. Feltesse [d], Z.Y. Feng [k], W. Flauger [†,e], M. Flieser [h], K. Gamerdinger [h], J. Gayler [e], L. Goerlich [b], M. Goldberg [k], R. Grässler [a], H. Greif [h], M. Haguenauer [j], L. Hajduk [b], O. Hamon [k], P. Hartz [c], R. Haydar [i], W. Hildesheim [k], N. Huot [k], M.A. Jabiol [d], A. Jacholkowska [i], M. Jaffre [i], H. Jung [a], C. Kiesling [h], H. Kolanoski [c], V. Korbel [e], M. Korn [c], W. Krasny [b], J.P. Kubenka [h], J. Kurzhöfer [c], H. Küster [e], J.F. Laporte [d], U. Lenhardt [c], P. Loch [e], D. Lüers [†,h], J. Marks [e], J. Martyniak [b], T. Merz [e], H.K. Nguyen [k], H. Oberlack [h], U. Obrock [c], C. Pascaud · S. Peters [h], K. Rauschnabel [c], P. Ribarics [h], M. Rietz [a], M. Rudowicz [h], V. Rusinov [g], N. Sahlmann [a], E. Sanchez [h], P. Schacht [h], V. Shekelyan [g], Y. Sirois [j], P. Staroba [l], H. Steiner [k], U. Straumann [n], J. Turnau [b], L. Urban [h], C. Vallee [k], M. Vecko [j,l], P. Verrecchia [d], G. Villet [d], D. Wegener [c], H.P. Wellisch [h], T.P. Yiou [k], J. Žáček [i,m], Ch. Zeitnitz [e]

[a] *III. Physikalisches Institut der RWTH, Aachen, Germany* [1]
[b] *Institute for Nuclear Physics, Cracow, Poland* [2]
[c] *Institut für Physik, Universität Dortmund, Dortmund, Germany* [1]
[d] *DAPNIA, Centre d'Etudes de Saclay, Gif-sur-Yvette, France*
[e] *DESY, Hamburg, Germany*
[f] *Institute of Experimental Physics, Slovak Academy of Sciences, Košice, Slovak Republic*
[g] *Institute for Theoretical and Experimental Physics, Moscow, Russian Federation*
[h] *Max-Planck-Institut für Physik, München, Germany* [1]
[i] *LAL, Université de Paris-Sud, IN2P3-CNRS, Orsay, France*
[j] *LPNHE, Ecole Polytechnique, IN2P3-CNRS, Palaiseau, France*
[k] *LPNHE, Universités Paris VI and VII, IN2P3-CNRS, Paris, France*
[l] *Institute of Physics, Czech Academy of Sciences, Praha, Czech Republic*
[m] *Nuclear Center, Charles University, Praha, Czech Republic*
[n] *Physik-Institut der Universität Zürich, Zürich, Switzerland* [3]

(Received 27 December 1993)

The performances of the H1 liquid argon calorimeter modules for the energy measurements and identification of electrons are studied with test data taken at CERN in the energy range 5 to 166 GeV. Various electron identification estimators exploiting global or detailed shower characteristics are studied and compared. The usage of impact position measurements is also discussed. A best combination of robust shower estimators leads typically to π-misidentification probabilities in the range 1.5 to 5.0×10^{-3} at 30 GeV for 95% electron detection efficiency. This further reduces to $\sim10^{-4}$ for these pions to be misidentified as electrons below 25 GeV.

† Deceased.

[1] Supported by the Bundesministerium für Forschung und Technologie, FRG, under contract numbers 6AC47P, 6DO57I and 6MP17I.
[2] Supported by the Polish State Committee for Scientific Research, grant No. 204209101.
[3] Supported by the Swiss National Science Foundation.

Introduction

The lead/stainless steel-liquid argon (LAr) calorimeter [1] of the H1 experiment [2] at the HERA ep collider is finely segmented to optimally recognize and measure electromagnetic (e.m.) showers. Some of the calorimeter modules were tested in their final designs

SSDI 0168-9002(94)00018-3

at CERN in 1989–1990 in an energy range not unlike that of the scattered electrons in deep inelastic scattering events at HERA. The aim was to derive energy calibration functions for electrons [3], hadrons and jets [4] and to study electron/hadron separation. Some early results concerning e/π separation were discussed in ref. [5]. Here, we present our complete results on e/π separation performances studied for four module configurations.

The test set-up, module configurations and data sets are presented in sections 2 to 4. The analysis and results are presented in section 5. Section 5.1 introduces a simple clustering algorithm which determines the measurement envelopes for electron-induced showers and electron isolation. The linearity and resolutions for electron energy measurements and the e/π separation results obtained from calorimetry information restricted to the electron envelope are presented in sections 5.2 and 5.3 while the separation performances obtained using all available information within the isolation cone are presented in section 5.4. In the context of the actual H1 experiment, different physics analysis applications may require different combinations of electron estimators exploiting global or detailed shower characteristics. Hence, various sets of calorimetric estimators are considered as well as combinations using the independent information on the direction of the incident particles.

2. Experimental set-up

The LAr modules were installed in a cryostat on the H6 beam line of the CERN North Area. The layout of the beam telescope and H1 detector configuration is shown in Fig. 1. The beam line was mostly operated in a tertiary mode [6] with mixed e^+ and π^+ in the energy range 10 to 80 GeV produced in a 1 m polyethylene secondary target and transported (Fig. 1 top) over 370 m up to the experimental zone (Fig. 1 bottom). In this mode, the π^+ beam fraction increases roughly linearly with energy from about $10 \pm 5\%$ at 10 GeV to $70 \pm 5\%$ at 80 GeV. The momentum spread controlled by the aperture of a pair of collimators (coll. 3 and 8 in Fig. 1) was kept to $\Delta P/P \lesssim 0.5\%$. The beam energies above 80 GeV are achieved by operating in a secondary mode.

For the data taking, the arrival of a beam particle was signalled by a coincidence between a pair of scintillators (B_1 and B_2 in Fig. 1 bottom), each having a thickness of 1.25 cm and a cross-section of 3×3 cm^2. The beam halo was rejected by asking for an anti-coincidence with a veto wall (VM) of scintillator counters. This together with an additional cut on the maximal signal in a ring scintillator limited the acceptance for the beam to a useful area of about $\pi \times 1.5^2$ cm^2.

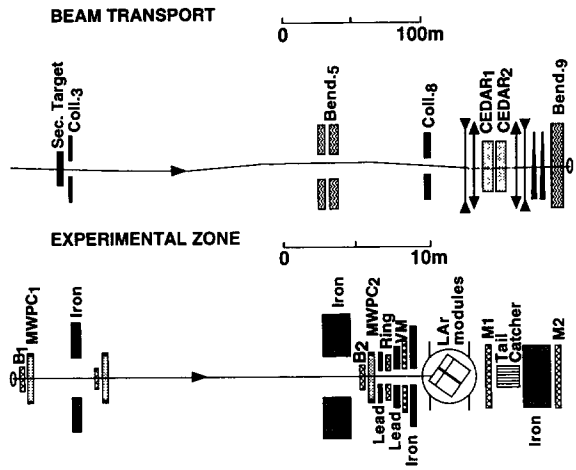

Fig. 1 Schematic representation of the beam transport (top) and H1 experimental set-up (bottom) during the CERN test runs. The small oval symbol marks the end of the vacuum beam pipe at the beginning of the experimental zone.

Two multiwire proportional chambers ($MWPC_{1,2}$) each with one horizontal and one vertical anode plane of wires were used to monitor the beam profile and to veto upstream showers. All planes had wire-to-wire spacing of 2 mm. $MWPC_2$ is placed at 1.9 m in front of the cryostat. The beam spot measured with the MWPC chambers has a $\sigma_x \sigma_y$ size varying from ~ 0.5 cm^2 at 10 GeV to ~ 0.2 cm^2 at 80 GeV.

The nature of the incoming particle was determined by the triggering in coincidence of two Cherenkov differential counters with achromatic ring focus (CEDAR) [7] which are well adapted to the above mentioned energy range in the tertiary mode, with a low energy operational limit for π's around 8 GeV due to the maximal allowed radiator gas pressure and an upper limit due to the minimal angular separation needed for the e and π Cherenkov rings around 95 GeV. Muons originating mainly from pion decay in flight were rejected by requiring an anti-coincidence with a scintillator veto wall (M2) placed behind the LAr cryostat after an additional 14 nuclear interaction lengths (λ_1) of material.

More details on the beam detectors and trigger system can be found in refs. [8,9], where test results of early prototype modules were presented.

3. Calorimeter modules configurations

The e and π single particle data were taken over four test periods each with a different pair of LAr modules having the materials, the read-out cell structure and the segmentation of the final H1 design [1]. Moreover,

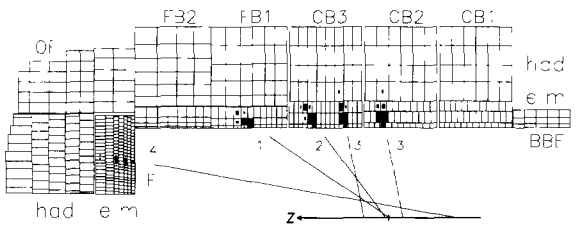

Fig. 2. Schematic representation of the impact directions in each of the four test configurations as viewed in the $r-z$ coordinates of half a cylinder of the H1 set-up at HERA. The line segments are drawn from the distance of closest approach to the z axis towards the calorimeter impact point.

as illustrated in Fig. 2, the impact points and angles were chosen to correspond to realistic conditions for similar modules in the full H1 set-up. In the three first periods (i.e. module configurations) an octant of two neighbouring central or forward barrel wheels, namely the FB1/FB2, CB3/FB1 and CB2/CB3 wheels, were put into the cryostat. In the fourth period, a quarter of the inner forward end-cap (IF) was used. As seen in Fig. 2, the segmentation of the electromagnetic (e.m.) and hadronic stacks varies from the CB to the IF wheel. Before penetrating the fiducial volume of the calorimeter stacks in the CERN set-up, the beam particles had to travel through 0.24 radiation length (X_0) of inactive material (air and beam detectors) up to $MWPC_2$, then $0.32X_0$ through the cryostat stainless steel entrance window, and finally through LAr and LAr-excluder (Rohacell) material; for a total of about $1X_0$ in the FB1/FB2 configuration, $0.8X_0$ for CB3/FB1, $0.7X_0$ for CB2/CB3 and $1.5X_0$ for IF. The main characteristics of the four types of modules which were hit by the incident beams at CERN are given in Table 1. For a given energy and module configuration, the electron and pion runs were taken at similar impact positions.

4. Signal processing and data sets

The electronic chain for the online treatment of the LAr pulses is described in detail in refs. [1,4,8]. Offline, all data are first pre-processed to bring the LAr signals to an "electromagnetic scale"; i.e. a scale corresponding to a calibration of both the e.m. and hadronic sections with electrons. The signal in each cell is corrected for pedestal offset and then converted from ADC counts to charge using a third order polynomial. The resulting charge is then corrected to take into account the cross-talk between calibration lines, leading typically to a few percent increase of the mean total charge for an e.m. shower. The charge is further corrected for eventual dead high voltage layers in some of the modules. Finally a time dependent correction is introduced to take into account a progressive decrease of the signal caused by pollution (outgassing from stack material or leakage from environment). For that, all runs of a given period are scaled to a common early point in time using factors determined by interpolating between 30 GeV "stability" runs taken under identical conditions throughout the period. In all cases, these factors correspond to a decrease of the charge of at most 2%.

In each period, the charge-to-energy calibration factors (about 3.6 GeV/pC) are determined first for the e.m. stacks, using electron data, by comparing the measured charge to the expected mean energy deposited within the fiducial volume of these stacks. The expected energy deposition is calculated by subtracting from each nominal incident energy the average losses in the beam elements and obstacles in front, as estimated by a detailed GEANT Monte Carlo procedure with very low tracking cuts. These energy dependent corrections represent at most a 0.5% decrease of the calibration factors. The calibration factors to bring the signal in the hadronic section to an electromagnetic

Table 1
Segmentation of the LAr modules. The mean Molière radius $\bar{R}_m$, radiation length $\bar{X}_0$, critical energy $\bar{\epsilon}_c$ and interaction length $\bar{\lambda}_I$ are given for the e.m. and hadronic sections. The mean longitudinal and lateral sizes of e.m. and hadronic (first layer) cells and the total number N_{cell}^{em} (N_{cell}^{had}) of e.m. (hadronic) cells in one "octant" ($\Delta\phi = 45°$) are given for each module. ΔL is the thickness of a layer and S the mean surface of a cell viewed at incidence normal to the front plane of the modules

Module	Electromagnetic section $\bar{X}_0 \simeq 1.6$ cm, $\bar{R}_m \simeq 3.6$ cm, $\bar{\epsilon}_c \simeq 9.5$ MeV, $\bar{\lambda}_I \simeq 31$ cm						Hadronic section $\bar{X}_0 \simeq 2.5$ cm, $\bar{R}_m \simeq 2.6$ cm, $\bar{\epsilon}_c \simeq 21.4$ MeV, $\bar{\lambda}_I \simeq 21$ cm			
	$\Delta L/\bar{X}_0$				$\sqrt{S}/\bar{R}_m$	Total N_{cell}^{em}	$\Delta L/\bar{X}_0$	$\sqrt{S}/\bar{R}_m$	No. of layers	Total N_{cell}^{had}
	$k=0$	$k=1$	$k=2$	$k=3$			$k=0$			
CB2	3.6	8.4	7.6	–	2.4	288	8.0	5.3	4	192
CB3	2.7	8.4	8.5	–	1.4	768	8.0	4.6	4	256
FB1	2.2	5.0	8.4	–	1.8	576	5.0	5.8	5	240
IF	3.0	5.4	7.2	13.0	1.0	≈ 1300	6.5	3.4	5	320

Table 2
Run configurations and the corresponding datasets. The e's and π's are impinging on the module printed in bold-face. The $z_{\mathrm{vtx}}^{\mathrm{H1}}$ are the mean z value of the point of closest approach to the beam axis in the H1 coordinates. The impact angles θ were chosen so that the modules entry face are orthogonal to the impact direction in the $x^{\mathrm{H1}}-y^{\mathrm{H1}}$ plane for configurations 1 to 3. In configuration 4, the entry face is at constant z^{H1}

Configuration	Module	$z_{\mathrm{vtx}}^{\mathrm{H1}}$ (cm)	θ	E (GeV)	N_{e}	N_{π}
1	**FB1**/FB2	1.8	34.3°	30	11197	38579
				80	1775	1445
				166	~ 1000	–
2	**CB3**/FB1	2.2	53.5°	5	~ 3000	–
				10	13254	2838
				20	5957	12997
				30	19360	20499
				40, 50	~ 3500	–
				80	~ 7000	–
3	**CB2**/CB3	−21.6	79.0°	10	3974	2020
				20	3788	4914
				30	1892	3204
				50	~ 2500	–
3	CB2/**CB3**	24.2	79.0°	10	3955	1786
				20	4371	3746
				30	10102	15754
				50, 80	~ 2500	–
4	**IF**	−34.1	10.1°	10	1313	1290
				15	~ 2000	–
				20	1192	1498
				30	2459	1490
				50, 166	~ 3000	–

scale are then deduced by extrapolation using Monte Carlo simulations to compare electrons starting directly at the entering plane of the electromagnetic and hadronic sections. Thus, the hadronic/e.m. ratios of the scaling factors are fixed to 2.1 for CBH/CBE and 2.0 for FBH/FBE and IFH/IFE [4]. The e/π separation analysis presented in sections 5.3 and 5.4 are performed at such an electromagnetic scale.

The e or π events are validated by requiring the firing of at least six PMs of each of the two upstream CEDARs and imposing that there be one and only one hit in each of the MWPC chambers. The validation requirements ensure at 30 GeV an upper limit on the π contamination probability in the e data well below 10^{-4} as could be checked by an unsuccessful search for events with abnormally low e.m. fractions ($< 10\%$) in the e-tagged data (about 50% of the π's at 30 GeV would satisfy such a cut). A similar figure is expected for the contamination of e's in the π-triggered data [7]. In the absence of an explicit cross-check, the π-rejection performances of the H1 LAr calorimeter presented in the following sections might nevertheless be considered as lower limits. Finally a minimal threshold of 1 GeV of total calorimeter energy is applied. This cut removes about 1% of true pions. The list of the datasets considered in the following analysis is given in Table 2.

5. Analysis and results

5.1. Clustering

We use a simple projective cone algorithm optimized for the measurement of e.m. showers. Taking as a seed the most energetic e.m. or hadronic cell in an octant, the group of four hottest contiguous cells (including the seed) is formed. A 6.5° cone is then opened around an axis passing through their common energy weighted centroid and the H1 equivalent vertex $z_{\mathrm{vtx}}^{\mathrm{H1}}$, starting from a distance of 1 m from the energy centroid (see Fig. 3). All cells having a geometrical centroid within this cone and an energy above $n_{\sigma}\sigma_{\mathrm{noise}}^{i}$ are kept as members of the cluster, where n_{σ} is a constant of order 1 and $\sigma_{\mathrm{noise}}^{i}$ is the energy equivalent of the rms electronic noise fluctuations in channel (cell) i measured in randomly triggered events. This noise corresponds typically (e.g. on average for CB3 cells) to 20 MeV (40 MeV) for e.m. (hadronic) cells and depends linearly on the cell volume.

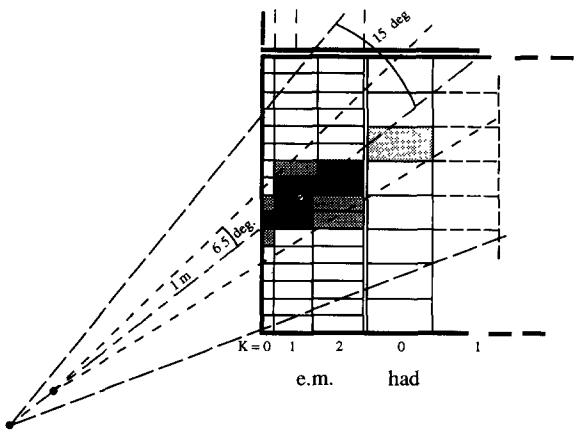

Fig. 3. Ingredients of the projective cone algorithm. The 6.5° cone contains the e.m. shower envelope and is surrounded by a 15.0° isolation cone which would essentially contain a hadronic shower.

The 6.5° *cluster cone* contains what we define as the *electromagnetic shower envelope* which comprises the e.m. cells and the ones of the first hadronic layer. Its opening angle was optimized for electron linearity and resolution performances (see next section). For e/π separation studies, we furthermore consider the leakage in an *isolation cone* starting at $z_{\mathrm{vtx}}^{\mathrm{H1}}$ with a 15.0° opening angle around the same principal axis as for the cluster cone. Except if mentioned otherwise, all e/π separation studies are done with an underlying noise cut (in units of $\sigma_{\mathrm{noise}}^{1}$) of $n_\sigma = 2.5$.

5.2. Resolutions and linearity

The opening angle $\Delta\psi$ of the clustering cone and the level n_σ of the noise suppression cuts have to be adjusted to ensure an optimal linearity with stable resolution performances. In the present case, given the quality requirements for deep inelastic scattering physics at the HERA collider, a deviation from linearity inferior to 1% is desired over the energy range from 5 to 166 GeV covered by the CERN test data.

The mean collected charge per unit energy measured inside the e.m. shower envelope with the CB3 module of configuration 2 (^{2}CB3) is plotted as a function of incident energy in Fig. 4 (top) for noise cuts varying from $n_\sigma = 1.0$ to $n_\sigma = 4.0$ (note the enlarged scale on the y axis). Given the asymmetric noise cut used in this analysis, the electronic noise adds on average in each channel layer a positive offset to the *physics induced* charge and plays an important role towards lower energies. For low noise cuts (e.g. $n_\sigma = 1.0$) an increasing excess of noise is kept with decreasing energy while on the contrary we suppress an increasing fraction of physics induced signal for a high noise cut (e.g. $n_\sigma = 4.0$).

The calibration factors are found to be only slightly dependent on the opening of the cluster cone for a cut $1.5 \le n_\sigma \le 2.5$ and for opening angles $5.0° \le \Delta\psi \le 7.0°$. The deviations from linearity for a 6.5° cone in the $n_\sigma = 1.5$ case are shown for all module configurations in Fig. 4 (bottom). In all cases, a deviation from linearity inferior to $\pm 1\%$ is achieved. It should be noted however that this excellent linearity partly results from a delicate *cancellation* between the loss in physical signal and the contribution of the noise within the fixed e.m. cluster envelope used here. Another approach using symmetric noise cuts and Monte Carlo extrapolations will be presented in a separate paper [3] where an absolute comparison of the electron calibration factors obtained for the various LAr modules will be discussed.

The energy resolutions achievable within the e.m. envelope of the clustering cone for a 6.5° cone and a $n_\sigma = 1.5$ noise cut applied on individual cells are obtained from Gaussian fits of the total energy distributions. The fits are performed on an asymmetric domain $[\langle Q\rangle - 1.5\sigma_{\mathrm{rms}}, \langle Q\rangle + 3\sigma_{\mathrm{rms}}]$ in order to be insensitive to low energy tails in electron data which are specific to the actual test data and are due to straggling in the dead materials along the beam line upstream from the calorimeter modules. These low energy tails are essen-

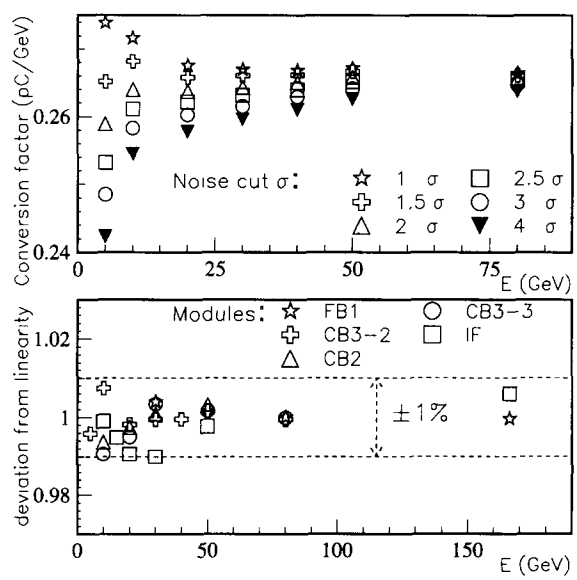

Fig. 4. Linearity performances of the H1 LAr modules for electrons measured with a projective cone cluster: (top) calibration factors in ^{2}CB3 for various noise cuts as function of incident energy; (bottom) deviations from linearity as a function of incident energy in each configuration for a cone opening of 6.5° and a $1.5\sigma_{\mathrm{noise}}$ cut.

tially independent of the energy and the test period and about 1.7% of the electrons are found below $\langle Q\rangle - 3\sigma_{\rm rms}$ (about 2.9% below $\langle Q\rangle - 3\sigma_{\rm Gauss}$). The χ^2 per degree of freedom of the Gaussian fits are in all cases excellent and vary between ~ 0.5 and ~ 1.5 with no systematic trend versus energy.

The measured resolutions obtained from electron data in each configuration in the energy range from 5 to 166 GeV was fitted with a function:

$$\frac{\sigma(Q)}{Q} = \frac{c_1}{E} \oplus \frac{c_2}{\sqrt{E}} \oplus c_3 = \frac{\sqrt{c_1^2 + c_2^2 E + c_3^2 E^2}}{E}, \qquad (1)$$

where c_2 represents the contribution from sampling fluctuations, c_1 the noise term and c_3 accounts for systematics and for the dispersion of the incident beam momenta.

The fits are illustrated in Fig. 5 in a σ/E vs. $1/\sqrt{E}$ plot for four modules in the three test configurations where we have data below 30 GeV. The values of the parameters c_1, c_2 and c_3 obtained for each module are given in Table 3. The cases where we have the largest number of data points, namely ^{2}CB3 and IF, were first fitted using the function (1) and three free parameters. The weighted mean average of c_3 was then imposed for the fits of CB2 and ^{3}CB3 data. Finally, c_1 and c_3 were imposed when fitting the FB1 data where we considered only three data points. The CB (and FB) data sets give mutually consistent results for each contribution to the energy resolution. We typically obtain a sampling contribution of $11\% \times \sqrt{GeV}$ and we are left, at *infinite* energies, with a constant term of 0.5% which is comparable to the incident beam momentum spread. A larger value of the sampling term c_2 is observed for the IF data which suffered from an additional 0.7–$0.8 X_0$ of dead material in front compared to the CB data.

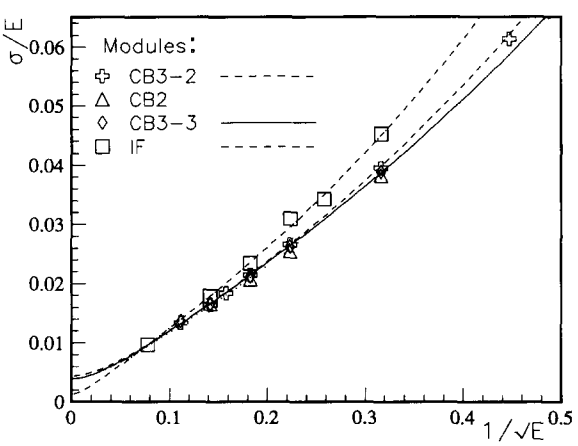

Fig. 5. Fractional charge resolution σ_Q/Q ($=\sigma_E/E$) vs. $1/\sqrt{E}$ for electron energies in the range 5 to 166 GeV for four LAr modules. The data are fitted to the resolution function (1) (see text).

Table 3
Results of the resolution function fits. Contributions of the noise term c_1, the sampling term c_2 and the "constant term" c_3 as well as the χ^2 per degree of freedom of the fits. All entries having quoted errors were left as free parameters in the fitting procedure

Stack	χ^2	c_1 (MeV)	c_2 ($\%\sqrt{GeV}$)	c_3 (%)
FB1	2.6	183	11.6 ± 0.3	0.47
^{2}CB3	0 17	188 ± 15	10.8 ± 0.3	0.51 ± 0.09
CB2	1.07	163 ± 24	10.8 ± 0.2	0.47
^{3}CB3	0.43	163 ± 21	11.0 ± 0.2	0.47
IFE	1.69	234 ± 35	12.1 ± 0.4	0.16 ± 0.24

5.3. Electron preselection within an e.m. shower envelope

We first study the e/π separation performances achievable within the (smallest) optimal volume for electromagnetic shower measurements. Hence we only consider the information from the electron shower envelope within the 6.5° cluster cone. Here we restrict to the cells in the e.m. section of that envelope neglecting the small leakage of electromagnetic showers in the hadronic section mostly due to weakly attenuated photons ($\lesssim 1\%$ on average for 30 GeV electrons in all configurations). Moreover, we do not assume, for the moment, that we have access to a priori information on incident momentum and impact point that could be provided by a tracking detector. These restrictions are motivated by applications in reconstruction algorithms which are often performed on a detector-by-detector basis and where an early (fast) independent tagging of potential electron candidates is desired.

5.3.1. Minimal requirements

We start by applying a set of minimal requirements on the electron and pion data which will be maintained throughout the analysis within the e.m. shower envelope. We ask for at least one firing cell in the first layer ($k=0$) of the e.m. section (i.e. $E_{k=0}/E_{\rm em} \neq 0$) and at least one additional cell in the e.m. section within the cluster cone (i.e. $E_{k=0}/E_{\rm em} \neq 1$). Moreover, in order to get rid of pions punching through the e.m. section, we require that the total energy measured in the e.m. section of the cluster cone satisfies $E_{\rm em} \geq 1$ GeV. Both requirements are satisfied by 100% of the electrons in all module configurations and for all incident energies considered. They lead, e.g. at 30 GeV, to π-rejection factors of $R_{e/\pi} = 1.7$ (FB1), 1.9 (^{2}CB3), 2.9 (CB2), 2.1 (^{3}CB3) and 1.7 (IF), where $R_{e/\pi}$ is defined as the ratio $R_{e/\pi} = \epsilon_e/\epsilon_\pi$ of the electron detection efficiency ϵ_e

over the probability ϵ_π to misidentify a pion as an electron. These factors vary linearly with incident π energy with a slope depending on the module configuration. They improve slightly towards lower incident energies reaching for instance at 10 GeV, 3.2 (CB2), 2.7 (^{3}CB3) and 1.8 (IF).

5.3.2. Global estimators

Within the volume defined by the electron shower envelope, we are interested in peculiarities of the e.m. showers. The ones which distinguish them best from hadronic showers are an early start characteristic of the X_0 scale for electron energy losses by bremsstrahlung and a compact hot core. Hence we can define simple preselection estimators based on the fraction of the e.m. energy which is deposited in the first e.m. layer ($E_{k=0}/E_{em}$) and the fraction of the energy contained in the "hot" core of the most energetic e.m. group of N contiguous cells which include the hottest cell (E_{hotN}/E_{em}). The N cells forming the core are allowed to belong to any of the first two e.m. layers ($k = 0$ or *1*) for the CB2, CB3 and FB1 modules or to any of the first three layers ($k = 0$, 1 or 2) for the IF module. This ensures in each case that the "core" contains the maxima of e.m. showers and remains safely below $1\lambda_I$ in depth for hadronic showers. The optimal numbers N of cells in the core were chosen in each configuration to optimize the e/π separation and to contain a similar mean fraction of the energy of an e.m. shower. We use $N = 4$ for CB2, 8 for CB3 and FB1, and 12 for IF such that $E_{hotN}/E_{em} \simeq 85$–$90\%$ for 30 GeV electrons (90–95% for 10 GeV electrons). Typical event densities for these estimators are shown in Figs. 6a and 6b for similar initial e and π populations at 30 GeV (^{2}CB3). The distributions are obtained

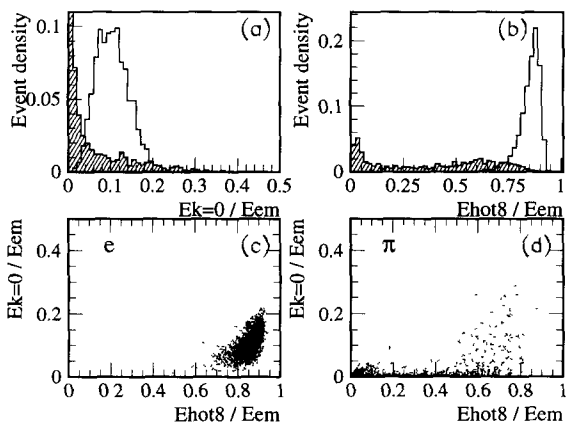

Fig. 6. Event density distributions for the estimators (a) $E_{k=0}/E_{em}$ and (b) E_{hot8}/E_{em} for e's (opened) and π's (hatched) at 30 GeV in ^{2}CB3. Correlation plots for these two estimators are shown in (c) for e and (d) for π.

after imposing the set of minimal requirements of section 5.3.1. Figs. 6c and 6d show correlation plots for electrons and pions respectively.

To calculate rejection factors, the estimators are combined on event-by-event via $x = (\ln E_{k=0}/E_{em}, E_{hotN}/E_{em})$ into a χ^2-like estimator making use of the full covariance matrix:

$$\xi^2 = (x - \bar{x})^T C^{-1} (x - \bar{x}) = \sum_{i,j} (x_i - \bar{x}_i) C_{ij}^{-1} (x_j - \bar{x}_j), \quad (2)$$

where $\bar{x}_i$ as well as the dispersions and correlations entering the calculation of the covariance matrix C are obtained from electron data and parametrized with energy. From this ξ^2 estimator, we obtain π-rejection factors (for a π of a certain incident energy to be misidentified as an electron at any measured energy) which are largely independent of incident energy in the 10 to 80 GeV range. We find for 30 GeV pions at $\epsilon_e = 99\%$ that $R_{e/\pi} = 8.0$ (FB1), 7.5 (^{2}CB3), 7.7 (CB2), 10.5 (^{3}CB3) and 25.4 (IF). The best rejection factors are obtained for IF which is the most finely segmented module and for which on event-by-event, the $N = 12$ cells of the E_{hotN}/E_{em} better match the true core of the e.m. showers.

5.3.3. Longitudinal shower shape

Given an approximate shower direction (taken for the moment as the cluster cone axis passing through a mean H1 equivalent vertex), we can make use of the a priori knowledge on the expected longitudinal shower shape under the electron hypothesis. In practice, this amounts, given a shower energy E measured in the e.m. envelope and distributed among cell layers, to calculate iteratively the parameters of a function describing the dE/dl shower shape and compare the obtained values with those expected for electrons at an incident energy of $E_{inc} = E$.

When integrating over coarse enough layers, i.e. $\Delta L \gg 1 X_0$, the mean longitudinal development of an e.m. shower is well described by the Longo–Sestili empirical formula [10]:

$$\frac{dE}{dl} = E_{inc} \frac{\beta^\alpha}{\Gamma(\alpha)} l^{\alpha-1} e^{-\beta l}, \quad (3)$$

where l is the shower depth in units of X_0 and α and β are energy dependent free parameters. This is seen for example in Fig. 7 for which the profile formula (3) (integrated over each layer) was fitted, using $a = 1/\alpha$ and $b = \beta/\alpha$ as free parameters, to the average energies measured in the three e.m. layers of ^{3}CB3 for electrons of $E_{inc} = 10$, 20 and 30 GeV. We obtain consistent values of the fit parameters at a given energy for different modules and impact angles. Averaging out the fit values (compatible within errors) found for ^{2}CB3 and ^{3}CB3, we obtain for example that $a =$

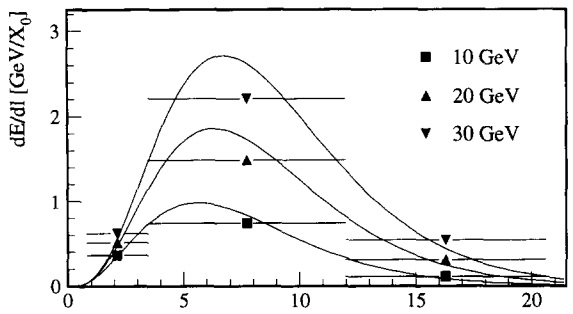

Fig. 7. Fits of the mean longitudinal shower energy density (per X_0 unit) profiles measured in the three e.m. layers of the ^{3}CB3 module for e at 10, 20 and 30 GeV.

$1/\alpha = 0.263$, 0.243, 0.232 (± 0.001) and $b = \beta/\alpha =$ 0.134, 0.122, 0.116 (± 0.001) for electrons of 10, 20 and 30 GeV respectively. This is in excellent agreement with the empirical formulae [11] of

$$\alpha \simeq \left(0.492 + \frac{2.38}{Z_{\text{eff}}}\right) \ln \frac{E_{\text{inc}}}{\epsilon_c} \tag{4}$$

and

$$\beta = \frac{\alpha - 1}{\ln(E_{\text{inc}}/\epsilon_c) - 1.3} \tag{5}$$

which were derived from a detailed GEANT simulation and for which the critical energy ϵ_c was given in Table 1 and the effective Z of the media in the e.m. section is $Z_{\text{eff}} \simeq 66.8$. Such formulae are used for the parametrization of e.m. showers in the fast simulation programs of H1.

The parameters a and b are related in a simple way to the first and second order moments of the shower:

$$b = \frac{1}{\langle l \rangle}, \quad a = \frac{\langle l^2 \rangle - \langle l \rangle^2}{\langle l \rangle^2}. \tag{6}$$

Eqs. (3) and (6) can be used as a basis for an iterative procedure to determine a and b on an event-by-event basis. We use the energy weighted first ($m = 1$) and second ($m = 2$) moments calculated over 3 layers (4 in the case of IFE data) as $\langle l^m \rangle = (\sum_{k=1}^{3} E_k l_k^m)/\sum_{k=1}^{3} E_k$. At first iteration, the depth l_k is given by the geometrical centroid of layer k; a and b are then deduced from Eq. (6) and put into Eq. (3). In subsequent iterations, l_k^m are evaluated taking into account the distribution of energy *within* layer k according to this shower profile shape, i.e.

$$l_k^m = \int_k l^m \frac{\mathrm{d}E}{\mathrm{d}l}(a, b)\, \mathrm{d}l \Big/ \int_k \frac{\mathrm{d}E}{\mathrm{d}l} \mathrm{d}l.$$

Updated values of a and b are calculated from the resulting shower moments using Eq. (6) and these

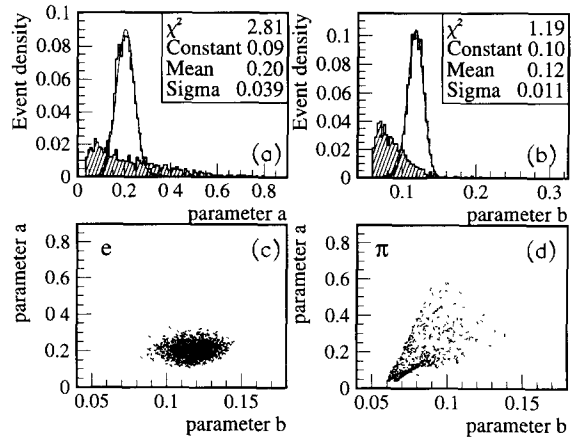

Fig. 8. (a,b) Event densities for the parameters a and b of the longitudinal shower shape for e's (opened) and π's (hatched). The e distributions are fitted to Gaussian functions. Correlation plots for these two parameters are shown in (c) for e and in (d) for π.

parameters are in turn put back into Eq. (3), and so on. After three iterations we obtain stable values of a and b (this is strictly true for electrons while for pions the procedure converges about half of the time). These are largely uncorrelated and Gaussian distributed for e.m. showers but rather flat for hadronic showers as seen in Figs. 8a and 8b. We can then build an estimator $\chi^2_{ab} \equiv (a - a_0)^2/\sigma_a^2 + (b - b_0)^2/\sigma_b^2$ by making use of the a priori knowledge of the mean a and b values and their dispersions as parametrized with energy using electron data. From that shower shape estimator, we obtain (Fig. 9a) similar rejection factors in all configurations, with values in the range $R_{e/\pi} \sim 5.5$ to 7.5 at $\epsilon_e = 99\%$ for energies in the range 10 to 30 GeV. The obtainable π-rejection further improves when rising the noise cut. This is seen for example in Fig. 9b in the case ^{3}CB3 where $R_{e/\pi}$ improves from ~ 6.3 at $n_\sigma = 2.5$ to 10.6, 9.2 and 8.2 for $E_{\text{inc}} = 10$, 20 and 30 GeV respectively at $n_\sigma = 8$. The a and b parameters for π's

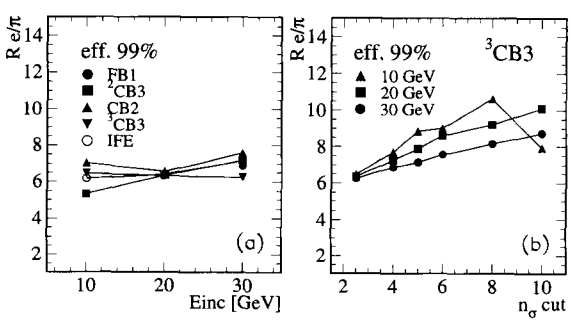

Fig. 9. Rejection factors $R_{e/\pi}$ for $\epsilon_e = 99\%$ obtained with the χ^2_{ab} estimator (a) vs. energy for all module configurations and (b) vs. the noise cut for CB3 in configuration 3.

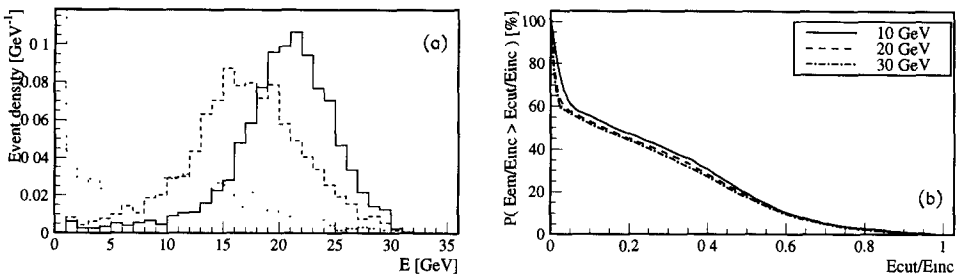

Fig. 10. (a) Distribution of the energies measured in the e.m. shower envelope (dotted), the cluster cone (dashed) and the isolation cone (solid) for 30 GeV π^+ and (b) hadronic opaqueness for 10, 20 and 30 GeV π^+, in ^{2}CB3 data.

are sensitive to the rise of the noise cut which mostly truncates peripheral cells in their shower expansion while the process leaves e shower parameters unaffected. Hence the χ^2_{ab} allows for (noise-dependent) π-rejection factors comparable to those obtained with the global estimators of section 5.3.2.

5.3.4. Hadronic opaqueness

The energy measurement restricted to the smallest volume containing the e.m. shower is optimal for performing e/π separation by the matching with an independent momentum estimator provided by a tracking detector. As can be seen for instance in Fig. 10a for 30 GeV pions at the e.m. calibration scale, the e.m. shower envelope is largely transparent to hadrons.

We define a measure of the non-transparency (opaqueness) as the probability that the fraction of the π incident energy $E_{\rm inc}$ recovered in the e.m. section within the 6.5° cone be above a threshold fraction $E_{\rm cut}/E_{\rm inc}$. This measure of the pion suppression power is shown in Fig. 10b for 10, 20 and 30 GeV pions impinging on CB3. The LAr e.m. section (hence the electron envelope) is seen to be almost as transparent at 10 GeV than at higher π energies. This can be understood given the fact that the fraction of the incident π^+ energy transferred to π^0's by the chain of inelastic interactions in the shower increases (logarithmically) with energy while the interaction length stays rather constant in the energy range considered.

5.4. Electron identification within the isolation cone

We now consider the electron identification performances using calorimetric information from the full isolation cone. This is particularly relevant in the context of H1 at HERA where the physics imposes the application of an isolation criterion for the scattered electron from deep inelastic collisions.

5.4.1. Global properties and longitudinal sampling

In the full isolation cone, we consider four preselectors. We again make use of the simple global properties introduced in section 5.3.2, namely the fraction of e.m. energy deposited in the first e.m. layer ($E_{k=0}/E_{\rm em}$) and the fraction contained in the hot core of the most energetic e.m. group of N contiguous cells ($E_{{\rm hot}N}/E_{\rm em}$). These can now be complemented by a powerful estimator relying on the longitudinal leakage of π showers in the hadronic section ($E_{\rm em}/E_{\rm tot}$) and by the fraction of energy leaking out transversely from the clustering cone within the "isolation" cone ($(E_{\rm iso}-E_{\rm tot})/E_{\rm tot}$); both of these being normalized to the total energy $E_{\rm tot}$ in the full 6.5° clustering cone (i.e. including cells of the hadronic sections). Typical event densities for these last two preselectors relying on properties of the hadronic shower expansion are shown in Figs. 11a and 11b. It should be noted that for π showers with large values of $E_{\rm em}/E_{\rm tot}$, this e.m. fraction is only weakly correlated with $E_{{\rm hot}N}/E_{\rm em}$.

It is interesting to study how the e.m. fraction estimator $E_{\rm em}/E_{\rm tot}$ can be, by itself, optimized by adjusting the thickness (in X_0 or λ_I) of the e.m. section. For that, we can profit from the longitudinal segmentation of the modules and particle penetration angles in order to vary the effective "e.m. section" length L over which $E_{\rm em}$ is integrated (notwithstanding the fact that the cell layer planes are actually not

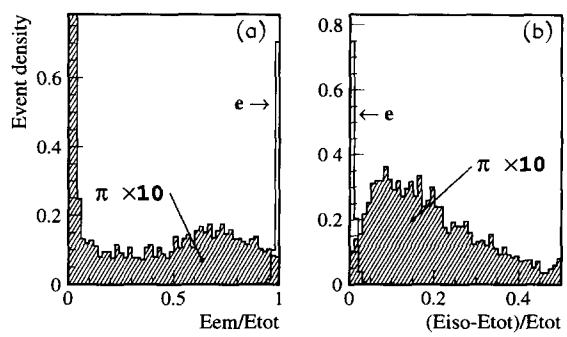

Fig. 11. Event density distributions for e's (opened) and π's (hatched) at 30 GeV in ^{3}CB3 for the estimators: (a) $E_{\rm em}/E_{\rm tot}$ and (b) $(E_{\rm iso}-E_{\rm tot})/E_{\rm tot}$.

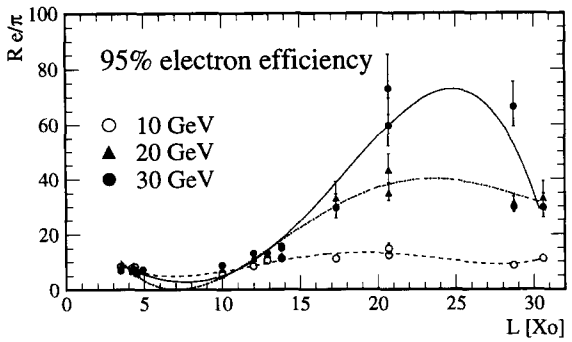

Fig. 12. π-rejection factors from longitudinal sampling vs. the e.m. section length L obtained at $E_{inc} = 10$, 20 and 30 GeV for $\epsilon_e = 95\%$.

perpendicular to the impact directions). The rejection factors obtained at fixed ϵ_e as a function of L are shown at 10, 20 and 30 GeV in Fig. 12 which cumulates the data of the various configurations. The optimal L can be seen to slightly increase with energy with a maximum around $L \approx \lambda_I$. The worse rejections are obtained for $L \approx 6X_0$, i.e. with an e.m. section ending around the e.m. shower maximum.

In order to calculate the rejection factors provided by a combination of parallel cuts on the four preselection estimators introduced above, we take into account the energy dependence of the cuts. This is necessary because we are here again interested in the rejection power for a π of a certain energy to be misidentified as an electron of *any* measured energy. The rejection factors obtained as a function of incident π energy from a combination of global properties within the isolation cone are shown in Fig. 13a. A simple combination of energy dependent cuts on $E_{k=0}/E_{em}$, E_{hotN}/E_{em}, E_{em}/E_{tot} and $(E_{iso} - E_{tot})/E_{tot}$ gives rejections rising from 0.5 to 1.1×10^2 at 10 GeV up to 0.9 to 3.1×10^2 at 30 GeV for $\epsilon_e = 97\%$. Comparable results are obtained when first combining $\ln(E_{k=0}/E_{tot})$ and E_{hotN}/E_{em} in a ξ^2-like estimator as in Eq. (2) (section 5.3.2). As trivially expected, the π's surviving the preselection cuts have a measured energy approaching that of electrons of the same incident energy. This can be seen in Fig. 13b.

5.4.2. Impact point matching

The impact point of an incident particle can be reconstructed along the axis passing through a vertex and the geometrical centroid of the calorimeter cluster, which we calculate here as the weighted sum $u = (\Sigma_{cells} u_i \sqrt{E_i})/\Sigma_{cells}\sqrt{E_i}$ with $u = (x, y, z)$ taking into account the energy shared among all cluster cells. For a single particle this point should match with the expected impact provided by an independent tracking detector. This impact point matching, which is generally limited by the quality of the position resolution for e.m. showers, is a powerful method to suppress overlap (e.g. $\gamma\pi^{\pm}$) contamination in single particle tagging. The position resolution of our various H1 LAr modules can be derived from CERN data by comparison with the impact point provided by the MWPCs.

From the last MWPC which provides an impact resolution of $\sigma \simeq 2$ mm$/\sqrt{12}$ in both horizontal (x_1) and vertical (y_1) directions, the beam particles have essentially parallel trajectories and, hence, the constant impact angles given in Table 2 in the H1 coordinates. A displacement in (x_1, y_1) can be translated on event-by-event into a displacement of the H1 equivalent vertex (i.e. the point at the distance of closest approach to the z^{H1} axis) from the mean values given in Table 2. The θ and ϕ angles sustained by the geometrical centroids of the clusters viewed from such vertices can then be compared to the nominal impact angles. The deviations are shown for example in Figs. 14a and 14b as a function of the MWPC coordinates of impact for 30 GeV e in ^{3}CB3. The systematic trends and extrema (e.g. in Fig. 14b) are due to the finite cell sizes and non-projectivity of their lateral boundaries. For this and for other configurations the dependence of the mean deviations on the impact can be simply parametrized and factored out. The remaining angular dispersions in θ and ϕ are Gaussian distributed as

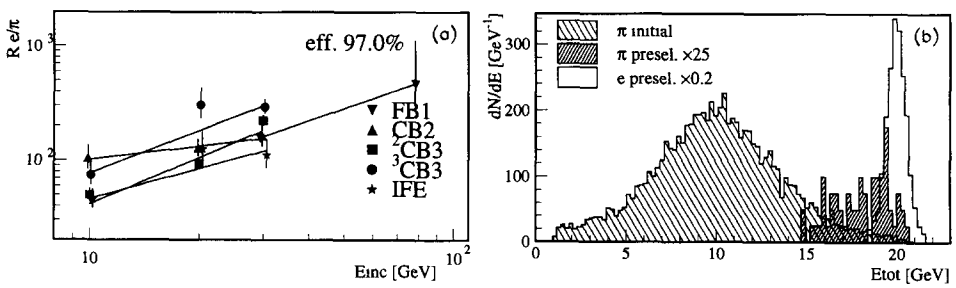

Fig. 13. (a) π-rejection factors from simple energy dependent cuts on four preselectors (see text) for all configurations and energies at $\epsilon_e = 97\%$. (b) The initial energy distribution (within the cluster cone) of pions (hatched) shrinks after preselection (dark ×25) approaching the electron one (opened ×0.2).

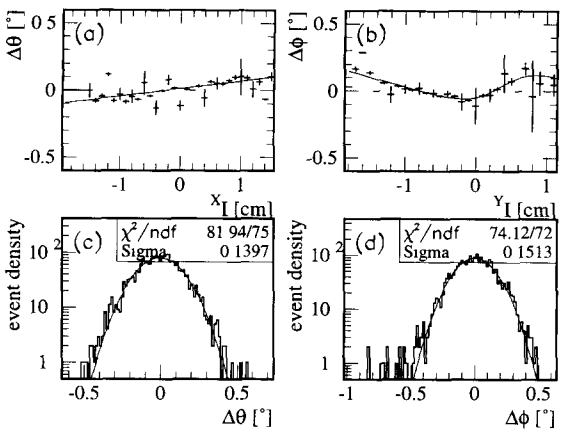

Fig. 14. Deviations of the reconstructed angles (a) θ and (b) ϕ from the nominal values as a function of the MWPC impact point; and angular dispersions from mean values in (c) θ and (d) ϕ fitted to Gaussian functions, for ^{3}CB3 data.

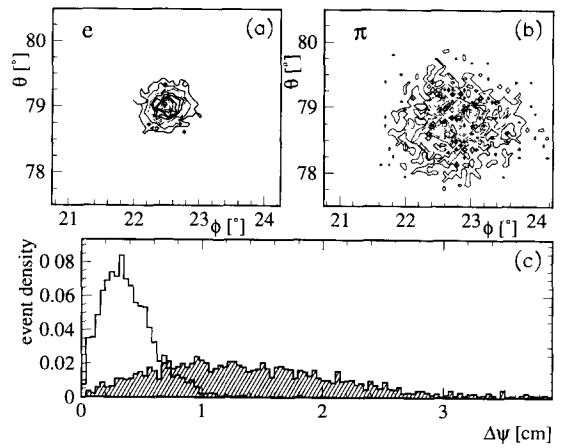

Fig. 16. Impact reconstruction in azimuthal (θ) and radial (ϕ) angles of (a) e's and (b) π's at 30 GeV in ^{3}CB3. (c) Frequency distributions for the distance deviation $\Delta\psi$ relative to the impact axis for e's (opened) and for π's (hatched).

shown for example in Figs. 14c and 14d for the ^{3}CB3 data.

The variation with incident energy of the spatial resolutions along θ, $u_\theta = D \tan \sigma_\theta$, and ϕ, $v_\phi = R \tan \sigma_\phi$, are plotted in Figs. 15a and 15b respectively. D and R are the mean distances and radii (see caption of Fig. 15) from the vertices to the modules front faces. These resolutions are seen to nicely scale in proportion to $1/\ln E$ and are found on average to vary from $\sigma(u_\theta) \simeq 0.37$ to 0.21 cm, and $\sigma(v_\phi) \simeq 0.40$ to 0.23 cm for energies ranging from 10 to 80 GeV. It should be noted that the incident beam profile here only scans a small fraction of a typical cell surface and that the spatial resolution for a given module depends on the impact point (as may be inferred for instance from the varying slope in Fig. 14b). Hence the differences between configurations in Fig. 15 cannot be generalized as representing average performances of the corresponding modules.

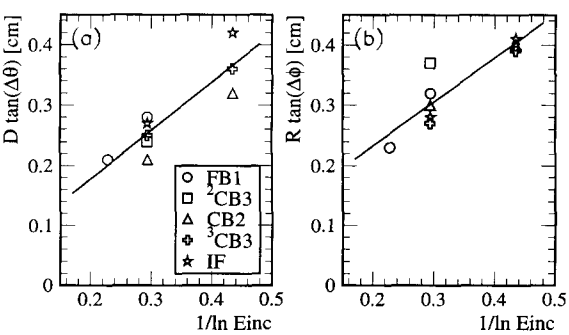

Fig. 15. Spatial resolutions (a) $D \tan \sigma_\theta$ and (b) $R \tan \sigma_\phi$ as a function of $1/\ln E_{inc}$. The distances D are 178.2 (FB1), 124.9 (^{2}CB3), 102.3 (CB2, ^{3}CB3) and 331.2 cm (IF). The radii R are 59.0 cm (IF) and 100.4 cm in all other cases.

Besides the application in overlap separation, the precision on the impact point reconstruction allows for a separation of single electrons and pions as was noted in ref. [12]. This has to do both with the differences in the scale of the lateral dispersions and with the fact that energy deposition in hadronic showers is less uniformly spread around the principal axis. The θ versus ϕ angular dispersions are shown for example in Figs. 16a and 16b for 30 GeV e's and π's in the ^{3}CB3 and the resulting deviation $\Delta\psi = ((\Delta u_\theta)^2 + (\Delta v_\phi)^2)^{1/2}$ from the nominal impact is shown in Fig. 16c. This $\Delta\psi$ can be used as an estimator for the e/π separation but its power diminishes as soon as one imposes in parallel a large e.m. fraction of energy f_{em} in the π showers via preselection requirements. Since the fraction f_{em} of the π shower energy which is deposited via π^0 components increases on average logarithmically with energy, we expect $\Delta\psi$ ln E_{inc} to scale linearly with f_{em} and to be roughly independent of E_{inc} at a given f_{em}. This is seen to be the case in Fig. 17a where the ratio E_{em}/E_{tot} is used as an estimate of f_{em}. The angular dispersion approaches that of electrons at large values of that ratio.

The gain in rejection factors when applying a cut on this angular dispersion $\Delta\psi$ on top of the requirement on the e.m. fraction E_{em}/E_{tot} is shown in Fig. 17b as a function of a threshold cut on E_{em}/E_{tot}. An improvement of the π-rejection of ~ 1.6 is even obtainable for $E_{em}/E_{tot} > 0.75$.

5.4.3. Separation from a minimal spanning tree

A measure of the topological characteristics of e.m. and hadronic showers can be derived from a minimal

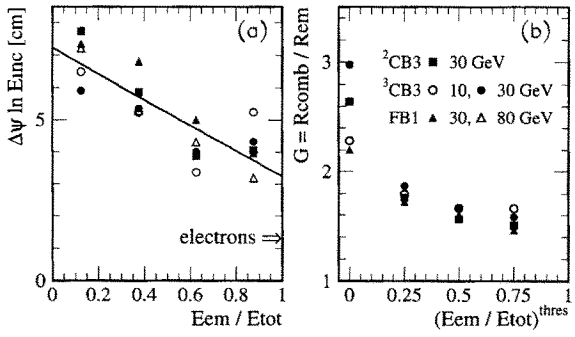

Fig. 17. (a) Scaled distance deviation $\Delta\psi$ ln E_{inc} as a function of the mean E_{em}/E_{tot} for π's in various configurations at three incident energies. (b) Gain $G = R_{comb}/R_{em}$ in the rejection (R_{comb}) obtained with a combined cut on $\Delta\psi$ and E_{em}/E_{tot} compared to the rejection (R_{em}) for a cut on E_{em}/E_{tot}, as function of a minimal requirement on E_{em}/E_{tot}.

spanning tree (MST) algorithm first borrowed from graph theory by the CHARM II Collaboration [13]. Here the spanning tree can be viewed as a multi-dimensional graph built up progressively by linking calorimeter cells. The links are weighted by a topological distance and the MST is that tree which minimizes the total weight (i.e. length) taken as the scalar sum of weights over all links. The tree can be developed starting from an arbitrary seed which we choose to be the hottest cell in the shower. Then the closest cell, according to the chosen metric, is linked and one iterates from there on, always adding the next closest cell to the growing tree until completion, i.e. until $N_{links} = N_{cells} - 1$. One MST solution is thus obtained. Its total length does not depend on the specific order in which the cells and links were examined.

The choice of the metric determines the MST building process. We consider the generalized distance between two cells

$$d_k = \sqrt{(c_G d_G)^2 - (c_E d_E)^2}, \tag{7}$$

where d_G is related to geometry and d_E to energy density with

$$d_G = \sqrt{(3 - 2w_r^2)(\Delta l)^2 + (w_r)^2(\Delta r)^2}, \tag{8}$$

where $w_r^2 = 3s^2/(2s^2 + 1)$, and

$$d_E = \sqrt{3}\,\Delta\rho/N_{cell}\bar{\rho}. \tag{9}$$

c_G and c_E in Eq. (7) as well as w_r in Eq. (8) are scaling factors. The differences Δl and Δr are measured longitudinally and transversely relative to the cluster principal axis. The distance d_G corresponds to an Euclidian distance if the dilatation factor s is set to 1. The $\Delta\rho$ in Eq. (9) is given by $\Delta\rho = (E_i/V_i - E_j/V_j)$ where $E_{i,j}$ and $V_{i,j}$ are the measured energies and volumes of cells i, j and $\bar{\rho}$ is the mean cell energy density.

Having built the MST, we consider as e/π estimators the total length of the tree $\mathscr{L}_{tot} = \Sigma_{links} d_k$, and the mean length of the links, $\Lambda = \mathscr{L}_{tot}/N_{links}$. We start by tuning a pure geometrical MST by setting $c_E = 0.0$ and vary the transverse dilatation s as well as the noise cut n_σ applied on individual cells. The noise cut affects the overall topology, and hence $\mathscr{L}_{tot}$ since it tends to suppress peripheral cells. The best π-rejection is obtained for $s = 5.0$ and $n_\sigma = 7.5$. The corresponding $\mathscr{L}_{tot}$ and Λ measured for 30 GeV e and π's in the ^{2}CB3 period are shown in Figs. 18a, 18b and 18c. Fixed values of N_{links} lead to a clusterisation along diagonal lines for π's in Fig. 18a. Both $\mathscr{L}_{tot}$ and Λ are Gaussian distributed for electrons and largely independent for pions.

The $\mathscr{L}_{tot}$ and Λ estimators can be combined on event-by-event into a ξ^2 estimator as in Eq. (2) with $x = (\mathscr{L}_{tot}, \Lambda)$. The π-rejection factors obtained for $s = 5$ at 30 GeV when comparing pions to electrons of the same incident energy are shown in Fig. 18d for a fixed noise cut $n_\sigma = 2.5$ with $c_E = 0.0$, 5.0 or 10.0, and for $c_E = 0.0$ with $n_\sigma = 2.5$, 7.5 and 10.0.

In the case of a purely geometrical tree (i.e. $c_E = 0.0$) with $s = 5.0$ and $n_\sigma = 2.5$, we obtain $R_{e/\pi} \simeq 15$ at $\epsilon_e = 97\%$. This improves to $R_{e/\pi} \simeq 25$ when introducing an energy component $c_E = 5.0$. Alternatively, it improves even more when rising the noise cut to $n_\sigma = 7.5$ which leads to $R_{e/\pi} \simeq 95$.

In order to compare our MST results with those of ref. [13], we exploit the distribution of the lengths of the links. We consider the frequency f^l of links having lengths within one of three possible bins ($1.0 \le d^1 < 2.0 \le d^2 < 3.0 \le d^3$) for showers having a given number

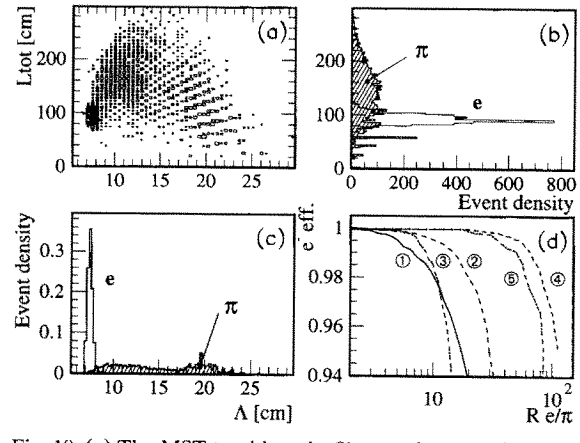

Fig. 18. (a) The MST total length $\mathscr{L}_{tot}$ vs. the mean length Λ for 30 GeV e's (closed boxes) and π's (open boxes) in ^{2}CB3 and the projections on (b) $\mathscr{L}_{tot}$ and (c) Λ obtained for $s = 5.0$ and $n_\sigma = 7.5$. (d) ϵ_e vs. $R_{e/\pi}$ for $s = 5.0$ with $n_\sigma = 2.5$ and (1) $c_E = 0.$, (2) $c_E = 5.0$ or (3) $c_E = 10.0$; ditto with $c_E = 0.$ and (4) $n_\sigma = 7.5$ or (5) $n_\sigma = 10.$.

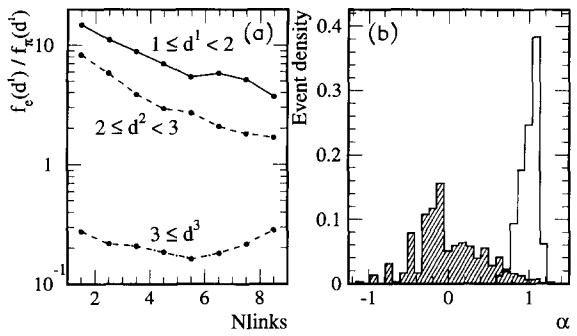

Fig. 19. (a) Ratio $f_e(d^i)/f_\pi(d^i)$ of the frequency of links of three different classes i for e and π, as a function of the total number of links for a noise cut $n_\sigma = 7.5$; (b) distribution of the "electromagneticity parameter" α for e's (opened) and π's (hatched) at 30 GeV in ^{2}CB3.

N_{links}. The e over π ratio f_e^i/f_π^i of frequencies is shown for each bin as a function of N_{links} in Fig. 19a. This information can be used on event-by-event basis to define a function

$$F(\alpha) = \sum_{i=1}^{2} \left[\left(f^i - \left[\alpha f_e^i(N_{\text{links}}) + (1-\alpha) f_\pi^i(N_{\text{links}}) \right] \right) / \sigma_e^i(N_{\text{links}}) \right]^2 \qquad (10)$$

that can be minimized as a function of α. Setting $\alpha = 1$, this reduces to the calculation of a χ^2-like estimator (with 2 degrees of freedom) which performs the comparison of the measured f^i to those expected for electrons. The event densities for the α which minimizes the function $F(\alpha)$ of Eq. (10) (an exactly solvable problem) is shown for 30 GeV ^{2}CB3 data in Fig. 19b. These compare very well with similar plots in ref. [13] and a combined cut on χ^2 and α typically lead to π-misidentification probabilities at the few percent level for $\epsilon_e = 97\%$. In that respect, the MST method does not favorably compete with the combination of preselection estimators introduced in section 5.4.1.

5.4.4. Shower moments and combined rejection factors

The fine granularity of the H1 LAr calorimeter offers the possibility to use both the longitudinal and lateral shower moments together with their correlations. We consider the first and second order moments calculated relative to the shower principal axis starting from its intersection with the entry plane of the calorimeter active volume. The moments are elements of the vector x:

$$x(1) = \langle l \rangle,$$

$$x(2) = \sqrt{\langle l^2 \rangle - \langle l \rangle^2},$$

$$x(3) = \langle r \rangle,$$

$$x(4) = \sqrt{\langle r^2 \rangle - \langle r \rangle^2},$$

$$x(5) = \langle rl \rangle - \langle r \rangle \langle l \rangle,$$

where $\langle l^n r^m \rangle = (1/\rho) \Sigma_{\text{cells}} \rho_i l_i^n r_i^m$ with the energy densities $\rho_i = (E_i/V_i)$ and $\rho = \Sigma_{\text{cells}} \rho_i$. The event density distributions for these moments are shown in Fig. 20 for 30 GeV e and π's of the ^{2}CB3 period. They are roughly Gaussian for electrons. The much larger spread of the π distributions reflects the differences between the electromagnetic (X_0 and R_m) and hadronic (λ_I) scales. Weighting by energy densities (instead of energy) renders the moments less sensitive to noise and enhances the relative contribution of the first e.m. layers. Distributions similar to those of Fig. 20 are obtained with energy weighting when rising the noise cut from the default $n_\sigma = 2.5$ to $n_\sigma \simeq 7.5$.

For the determination of π-rejection factors, we consider a combination of the cuts on the preselection estimators introduced in section 5.4.1 with a ξ^2 exploiting the full 5×5 covariance matrix of shower moments, following the recipe described in Eq. (2). Simi-

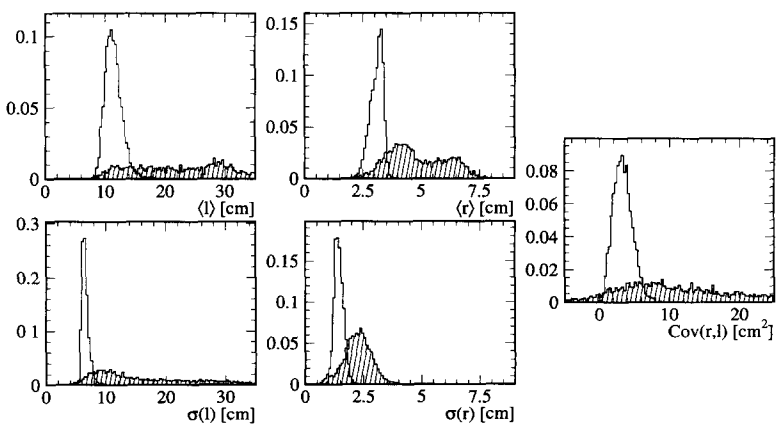

Fig. 20. Shower moment distributions for e's (opened) and π's (hatched) measured with the ^{2}CB3 module at 30 GeV.

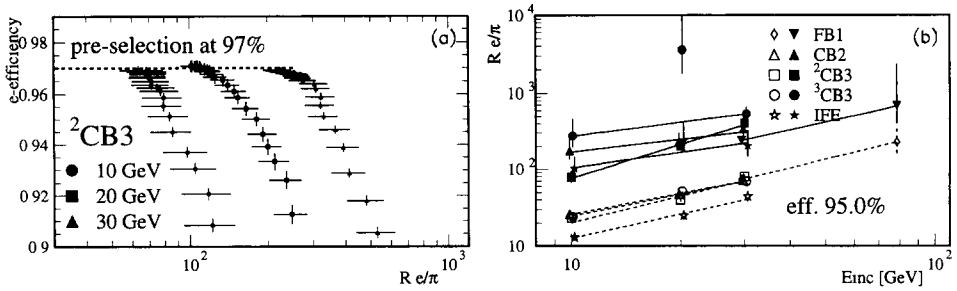

Fig. 21. (a) ϵ_e vs. $R_{e/\pi}$ for three energies in the ^{2}CB3 module. (b) $R_{e/\pi}$ at $\epsilon_e = 95\%$ as a function of π incident energy, obtained by combining preselection and the ξ^2 of the shower moments for all configurations (full symbols). The open symbols show $R_{e/\pi}$ obtained using only longitudinal estimators. The data of each module configuration are fitted to a straight line.

lar ξ^2 estimators, but relying on huge matrices involving as many elements as calorimeter cells, were introduced for e/π discrimination by refs. [14,15] and used by the D0 Collaboration for their uranium/LAr calorimeter [16]. The averages and dispersions of the shower moments as well as all other ingredients of the covariance matrix must first be parametrized as a function of electron energy. Obviously, the cuts relevant for an incident π of a certain measured energy E^π are those of an electron of incident energy $E^e_{inc} = E^\pi$. All parameters are found to vary slowly with energy and can be parametrized as a linear function of ln E^e_{inc}. After preselection, the correlations between "pure" longitudinal (i.e. $x(1)$ or $x(2)$) and "pure" transversal (i.e. $x(3)$ or $x(4)$) components of x are rather weak with linear correlation coefficients within ± 0.2. Applying a Pearson's test to the density distribution of the ξ^2 estimator for electrons, we find as expected that it is compatible with a χ^2 distribution with ~ 5 (i.e. the rank of the covariance matrix) degrees of freedom.

The variation of the π-rejection factors as function of the ϵ_e are shown in Fig. 21a for 10, 20 and 30 GeV π's in ^{2}CB3. The rejection factors finally obtained at $\epsilon_e = 95\%$ for the full combination preselection plus shower moments estimators are shown in Fig. 21b. The rejections obtained, which rise from $\sim 10^2$ at 10 GeV to $\sim 10^3$ at 80 GeV, are compatible with those obtained by D0 [16] and, for equivalent cell granularity, by Engelmann et al. [15]. Similar shower moment analysis of some of the H1 CERN data sets were discussed in refs. [5,11,17] reproducing with good agreement the results presented here. The π-rejection that would be obtained in absence of any transversal segmentation of our modules can be studied here by using only the longitudinal preselectors (i.e. $E_{k=0}/E_{em}$ and E_{em}/E_{tot}) and the first two elements of the vector x. The results are also shown in Fig. 21b. The rejection factors obtained are remarkably stable for the various configurations and vary smoothly with π incident energy. The IF module is slightly disfavoured here by the thickness of the first e.m. layer and the length (about $\sim 30X_0$ including dead materials in front) of the e.m. section. By comparing to the full combination, the transversal segmentation and the measurement of the transverse leakage of energy outside the cluster cone are seen to bring an improvement of ~ 4 (e.g. for FB1) to ~ 10 (e.g. for IF) of the π-rejection.

The π's surviving the combined preselection and shower moments rejection at a given ϵ_e, are strongly peaked toward their nominal incident energy, as was already seen after preselection in Fig. 13b. That is to say that, as expected, it is much more difficult using pure calorimetric estimators to distinguish π's from e's when $E^\pi/E^\pi_{inc} \simeq 1$. Nevertheless, the π-rejection can be further improved, especially towards low energy, if the information on incident particle momenta is provided independently by a tracking detector. This was studied indirectly for the FB1 data in ref. [18] by introducing the measured total energy density ρ as an additional element of x assuming that its strong dependence on incident momenta could be parametrized. This together with a full likelihood analysis comparing estimators of 30 GeV incident π's only to those expected for 30 GeV e's (independently of the measured

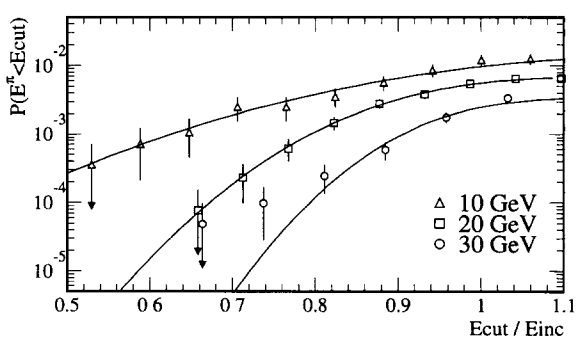

Fig. 22. Contamination probability $P(E^\pi < E_{cut})$ for a π of energy E_{inc} to be misidentified as an e with energy below E_{cut}, as a function of E_{cut}/E_{inc} for ^{2}CB3 data at 10, 20 and 30 GeV.

π energy) gave rejection factors well above 10^3 at $\epsilon_e = 95\%$.

For various physics applications, one is interested not only in the π-rejection for a π of a given energy to be accepted (i.e. misidentified) as an e at *any* measured energy as calculated in Fig. 21b, but also at the resulting π contamination *as a function* of the measured energy. The evolution with measured energy of the remaining π contamination is very similar for the various data sets, and shown for example in Fig. 22 for ^{2}CB3 data at 10, 20 and 30 GeV. The π-misidentification probability falls below 10^{-4} for $E^{\pi}/E^{\pi}_{inc} \lesssim 0.7$ above 20 GeV. Beyond that, the essentially indistinguishable contamination of charge exchange reactions $\pi^+ n$ to $\pi^0 p$ occurring in the first ($k = 0$) e.m. layer starts to contribute significantly.

6. Conclusions

A study in H1 LAr calorimeter modules of electron energy measurements in the range 5 to 166 GeV, and electron identification in the energy range 10 to 80 GeV was presented.

Within an e.m. clustering envelope adapted to the characteristic size of electromagnetic showers, electrons are found to be measured with a fractional sampling resolution of $\sigma_E/E \simeq 11\%/\sqrt{E}$ and π-misidentification is suppressed to the $\sim 10^{-1}$ level (at $\epsilon_e = 99\%$) by the requirements of an early shower start, the presence of a dense energetic core or a proper longitudinal profile shape.

This contamination is further reduced by exploiting the hadronic shower leakage out of the electron envelope. In an isolation cone adapted to the characteristic size of hadronic showers, a combination of preselection requirements, such as a large energy deposition in the e.m. section of the modules, leaves a π-misidentification at the $\lesssim 10^{-2}$ level (for $\epsilon_e = 97\%$). A π-misidentification at the $\sim 10^{-2}$ level ($\epsilon_e = 97\%$) is obtained with a Minimal Spanning Tree algorithm. A full combination of first and second longitudinal and transversal shower moments on top of the preselection requirements diminishes further the probability for, e.g., 30 GeV pions to be misidentified as electrons of any measured energy to $\sim 2 \to 5 \times 10^{-3}$ ($\epsilon_e = 95\%$). This probability falls to $\lesssim 10^{-4}$ for π's of energy E_{inc} to be misidentified as electrons at measured energy $E \lesssim 0.7\ E_{inc}$.

Acknowledgements

We wish to thank all technical collaborators who contributed to the construction and maintenance of the LAr calorimeters. The support of the CERN staff operating the H6 beam line is gratefully acknowledged. Finally, we thank all funding agencies for financial support.

References

[1] H1 Calorimeter Group, B. Andrieu et al., Nucl Instr. and Meth. A 336 (1993) 460.
[2] H1 Collaboration, I. Abt et al., The H1 detector at HERA, DESY preprint 93-103 (1993).
[3] H1 Calorimeter Group, Calibration of the H1 liquid argon calorimeter with electrons, in preparation.
[4] H1 Calorimeter Group, B. Andrieu et al., Nucl. Instr. and Meth. A 336 (1993) 499.
[5] H1 Calorimeter Group, B. Andrieu et al , Proc. 3rd Int. Conf. on Advanced Technology and Particle Physics, Como, Italy, June 1992, Nucl. Phys. (Proc. Suppl.) B 32 (1993) 97.
[6] P. Coet, CERN EBS note 85-14; See also H.W. Atherton et al., CERN SPS note 85-43.
[7] C. Bovet et al., CERN yellow report 82-13 (1982).
[8] H1 Calorimeter Group, W. Braunschweig et al., Nucl Instr. and Meth. A 265 (1988) 419.
[9] H1 Calorimeter Group, W. Braunschweig et al., Nucl. Instr. and Meth. A 270 (1988) 334.
[10] E. Longo and I. Sestili, Nucl. Instr and Meth. 128 (1975) 283
[11] S. Peters, Dissertation, Hamburg, MPI-PHE 92-13 (1992).
[12] B. Michel (ALEPH Collaboration), Nucl. Instr. and Meth. A 263 (1988) 43.
[13] CHARM II Collaboration, K. De Winter et al , Nucl. Instr. and Meth. A 277 (1989) 170.
[14] A. Babaev et al., Nucl. Instr. and Meth. 160 (1979) 427.
[15] R. Engelmann et al., Nucl. Instr. and Meth. 216 (1983) 45.
[16] S. Abachi et al., D0 Collaboration, Nucl. Instr. and Meth. A 324 (1993) 53.
[17] V. Boudry, Thèse de Doctorat, Université Paris VI (1992)
[18] M. Colombo, Diplomarbeit, Universität Dortmund (1990).